

To appear in ApJ

Observations of Global and Local Infall in NGC 1333

Andrew J. Walsh, Tyler L. Bourke, Philip C. Myers

*Harvard-Smithsonian Center for Astrophysics, Mail Stop 42, 60 Garden Street, Cambridge,
MA, 02138, USA*

awalsh@cfa.harvard.edu

ABSTRACT

We report “infall asymmetry” in the HCO^+ (1–0) and (3–2) lines toward NGC 1333, extended over $\sim 0.39 \text{ pc}^2$, a larger extent than has been reported before, for any star-forming region. The infall asymmetry extends over a major portion of the star-forming complex, and is not limited to a single protostar, or to a single dense core, or to a single spectral line. It seems likely that the infall asymmetry represents inward motions, and that these motions are physically associated with the complex. Both blue-asymmetric and red-asymmetric lines are seen, but in both the (3–2) and (1–0) lines of HCO^+ the vast majority of the asymmetric lines are blue, indicating inward motions. The (3–2) line, tracing denser gas, has the spectra with the strongest asymmetry and these spectra are associated with the protostars IRAS 4A and 4B, which most likely indicates a warm central source is affecting the line profiles. The (3–2) and (1–0) lines usually have the same sense of asymmetry in common positions, but their profiles differ significantly, and the (1–0) line appears to trace motions on much larger spatial scales than does the (3–2) line. Line profile models fit the spectra well, but do not strongly constrain their parameters. The mass accretion rate of the inward motions is of order $10^{-4} \text{ M}_{\odot}/\text{yr}$, similar to the ratio of stellar mass to cluster age.

Subject headings: stars: formation—ISM: clouds—ISM: kinematics and dynamics

1. Introduction

In the last few years mm-wavelength observations of infall asymmetry – the red-shifted self-absorption of optically thick spectral lines – have revealed evidence of inward motions in

starless cores, in cores with single embedded stars, and in small cluster-forming complexes, such as NGC 1333 and Serpens (Myers, Evans & Ohashi 2000, and references therein). In cores with single stars the infall asymmetry is usually localized (<0.1 pc), and is well matched by the standard model of “inside-out” gravitational collapse (Shu 1977) on scales 0.01-0.1 pc (e.g., B335 - Zhou 1995; L1527 - Mardones 1998; Wilner, Myers & Mardones 1997; Myers et al. 1995; SMM4 - Narayanan et al. 2002; Ward-Thompson & Buckley 2001; IRAM04191 - Belloche et al. 2002). This is in contrast to starless core maps which show that the infall is much more extended (0.1-0.3 pc) than is predicted by the standard model (Lee, Myers & Tafalla 2001). The cause of these extended motions is unclear, and models based on pressure-driven flows, dissipation of turbulence, supercritical magnetic infall, and early collapse from a condensed initial state have been proposed (Myers & Lazarian 1998; Nakano 1998; Ciolek & Basu 2000; Myers 2005).

Such extended infall asymmetry – global infall – is also seen in limited maps of small-cluster forming regions. For example, Williams & Myers (2000) report extended infall asymmetry in Serpens covering a region about 0.2 pc across, and Williams & Myers (1999) surveyed 19 young stellar clusters, but find extended infall towards only one: Cepheus A. Also, toward NGC 1333 IRAS 4 there are two main centers of gravity, 4A and 4B, both being multiple systems. They are separated by 0.05 pc, but infall asymmetry is observed over a larger area and encompasses both sources, with inferred inward speeds of 0.1 km s^{-1} (Mardones 1998). When observed with high resolution (H_2CO with $17''$ – Mardones 1998; HCO^+ with $10''$ – Choi et al. 1999; H_2CO with $2''$ – Di Francesco et al. 2001), IRAS4 also shows local infall centered on the protostars, as indicated by large blue-red ratios in the self-absorbed line profiles, within 0.02 pc. At the finest resolution these appear as inverse P-Cygni profiles.

One explanation for this observation is that the large scale flow results from a condensation process, while the small scale flow is due to gravitational collapse. In one model, the dissipation of turbulence due to ion-neutral damping of MHD waves, leads to an inward pressure gradient and inward flow along magnetic field lines (Myers & Lazarian 1998). Alternatively, the motions could be due to gravitational attraction by an extended layer or network of filaments. Another possibility is that the large-scale motions are a poorly-resolved superposition of many localized collapses.

NGC 1333 is a nearby reflection nebula in the Perseus molecular cloud complex (e.g., Bachiller & Cernicharo 1986). It is a busy region of star formation, containing many Class 0 sources (e.g., IRAS 4A, 4B, 2A, 2C and SVS 13B), as well as more evolved protostars. Assuming a distance of 300 pc, using Hipparcos data (de Zeeuw, Hoogerwerf & de Bruijne 1999; Belikov et al. 2002) NGC 1333 covers approximately a square parsec. Most of the young stars and protostars appear to be concentrated into a northern and southern cluster,

separated by about 5 arcminutes, equivalent to 0.4 pc. Together, the clusters contain at least 143 stars (Lada, Alves & Lada 1996).

As part of a survey of nearby clusters and groups, extended infall asymmetry was observed over a large part of the NGC 1333 region. In this paper we report on observations of extended infall in NGC 1333, in the lines of HCO^+ (1–0) and (3–2), and N_2H^+ (1–0).

2. Observations

2.1. FCRAO Observations

Observations with the Five College Radio Astronomy Observatory (FCRAO) were conducted on 2002, November 16. An area of approximately $16' \times 16'$ was mapped in the lines of HCO^+ (1–0) and N_2H^+ (1–0), covering all of NGC 1333. The region was mapped using an on-the-fly technique with the new 32 element array SEQUOIA, sampling every 0.25 beam, to produce a fully sampled map (FCRAO beam is $52.5''$ at the N_2H^+ (1–0) frequency) in 9 hours. The data were regridded onto a $26''$ grid to match up with the CSO observations detailed below. The bandwidth was 25 MHz over 1024 channels, giving a channel spacing of $\sim 0.08 \text{ km s}^{-1}$. Typical system temperatures were 160 to 180 K for both transitions. Typically, rms noise estimates are 0.05 K per channel in the center of each map, increasing to 0.08 K towards the edges of the mapped region. The rest frequency for N_2H^+ (1–0) was chosen to be 93.173258 GHz for the ‘isolated’ hyperfine component (Lee et al. 2001) and the rest frequency for HCO^+ (1–0) was chosen to be 89.188526 GHz (Pickett et al. 1998).

2.2. CSO Observations

Observations with the Caltech Submillimeter Observatory (CSO) were conducted from 2003, September 14 to 18. Maps of the southern half of NGC 1333, including SVS 13, IRAS 4 and IRAS 2, were made in HCO^+ (3–2). All maps were made on a $26''$ grid which is approximately beam spaced. Each pointing was observed with a 50 MHz bandwidth across 1024 channels, giving $\sim 0.05 \text{ km s}^{-1}$ channel spacing, and was observed in a chopping mode with 10 minutes on/off source time. The assumed rest frequency of HCO^+ (3–2) is 267.55762 GHz (Pickett et al. 1998) and typical system temperatures were 440 to 530 K.

3. Results

The $\text{HCO}^+(1-0)$ and $\text{N}_2\text{H}^+(1-0)$ FCRAO data are summarised in Figure 1. In all subsequent figures and discussion, offsets are relative to 03 29 03.9 +31 15 18.9 (J2000). Figure 2 shows three example spectra, including the optically thin line $\text{N}_2\text{H}^+(1-0)$, showing blue-shifted asymmetry, red-shifted asymmetry and no clear asymmetry. From an inspection of the $\text{HCO}^+(1-0)$ spectra in Figure 1, it is clear that many show blue-shifted asymmetric profiles (“infall asymmetry”). Furthermore, the optically thin $\text{N}_2\text{H}^+(1-0)$ emission maximum lies between the two $\text{HCO}^+(1-0)$ peaks, indicating that the HCO^+ profiles are likely due to inwardly moving gas that is self-absorbed. To show this more clearly, we color-code the HCO^+ spectra in Figure 3 where blue and red spectra indicate blue- and red-shifted asymmetry, respectively. We determine the color of each spectrum by using the method pioneered by Mardones et al. (1997), with δv defined as $(V_{\text{thick}} - V_{\text{thin}})/\Delta V$, where V_{thick} is the peak velocity of the optically thick line (HCO^+), V_{thin} is the peak velocity of the optically thin line (N_2H^+) and ΔV is the FWHM of the optically thin line. When $\delta v > 0.25$ we assign the spectrum to be red, when $\delta v < -0.25$ we assign the spectrum to be blue and when $-0.25 < \delta v < 0.25$, we assign the spectrum to be green.

The blue-shifted asymmetry is seen covering a large area ($\sim 0.3 \text{ pc} \times 0.2 \text{ pc}$), including most of the area between the star-forming regions IRAS 4, SVS 13 and IRAS 2. Towards SVS 13, the asymmetry appears to reverse, suggesting significant outward motions in this region, perhaps as a result of the well studied outflows (Knee & Sandell 2000). To the north-west of NGC 1333, a second area of extended blue-shifted asymmetry is seen, covering an area of $\sim 0.2 \text{ pc} \times 0.2 \text{ pc}$, near the source IRAS 5. The two areas join close to SVS 13 and together cover most of a region $0.85 \text{ pc} \times 0.5 \text{ pc}$, totaling an area of 0.39 pc^2 .

The $\text{HCO}^+(3-2)$ CSO data are compared to the $\text{HCO}^+(1-0)$ FCRAO data in Figure 4. The vertical lines are the systemic velocity determined by fitting the seven $\text{N}_2\text{H}^+(1-0)$ hyperfine line components at each position, using the HFS routine of CLASS¹. Most of the spectra in this figure show blue-shifted asymmetric profiles where there appear to be two peaks, the blue being stronger and the N_2H^+ line located in between the two HCO^+ peaks. Again, around SVS 13, the asymmetry reverses. Whilst this occurs in both the (1-0) and (3-2) lines of HCO^+ , it does not occur at the same positions for each line, e.g., the (0,0) position. The blue-shifted asymmetry appears to be most pronounced around IRAS 4, where inverse P-Cygni profiles have previously been reported (Choi et al. 1999; Di Francesco et al. 2001).

¹<http://www.iram.fr/IRAMFR/GILDAS>

4. Discussion

4.1. The Nature of the Extended Infall Asymmetry

We interpret the blue-shifted asymmetric profiles as infall asymmetry. The extended areas of infall asymmetry seen in Figures 1 and 4 cover much larger areas than previously mapped in regions of isolated star formation (Lee et al. 2001). Therefore, a new interpretation of these apparent inward motions may be required. One possibility is that the single dish observations are of such a low resolution that we observe a superposition of many sites of local infall over such a large area. This might be the case because NGC 1333 is a busy region of star formation presumably with many sites of localised infall. However, we consider this an unlikely cause of the observed extended inward motions for three reasons. First, the CSO observations are of moderately-high resolution and so are less likely to suffer from the same confusion problems as the FCRAO observations, and yet we still see similar infall profiles in both sets of observations covering the same area. Second, some positions are where no known star formation is taking place, e.g., $52''$ south of the center position. Third, to observe infall profiles over such a large area (>0.2 pc) would require a large number of localized infall regions aligned in such a way as to not leave any gaps (ie. regions without infall profiles), which would require an unlikely arrangement. Therefore we favor the explanation that the infall is physically different from local infall previously observed, and traces a global inward motion around many sites of local star formation.

Myers & Lazarian (1998) suggest that extended infall signatures may be the result of “turbulent cooling flows” associated with dissipation of turbulence. However, these models are mainly aimed towards explaining extended infall around isolated low mass star forming regions. One major difference between the theoretical work and our observations is that the infall speed modeled around isolated low-mass cores is subsonic, of order 0.1 km s^{-1} , whereas we measure supersonic infall speeds more like 0.5 km s^{-1} over extended areas (see §§4.5). It is not clear at this stage whether the models of Myers and Lazarian can be extended to such high infall speeds.

Walsh et al. (2004) calculate that speeds of 0.1 km s^{-1} can be achieved by gravitational attraction of test particles onto the NGC 1333 star forming complex in as little as 0.02 Myr, based on the mass of NGC 1333: $1450 M_{\odot}$, which was derived from CO measurements (Ridge et al. 2003). This is assuming that a test particle starts from rest and falls onto a point mass where gravity is the only force (ie. no pressure retarding the motion). Extending this calculation to infall speeds of 0.5 km s^{-1} , we expect speeds of this order to be reached in 0.1 Myr, which is about a tenth of the age of the cluster. This is consistent with global inward motions of gas falling into the dense centers of NGC 1333. On the other hand, this

model is extremely idealised and neglects the complex structure and motions of the region.

4.2. Infall modeling

We have attempted to model physical parameters associated with both the $\text{HCO}^+(1-0)$ and $(3-2)$ spectra. To do this, we have chosen a position (located at $0''$, $-52''$) that is relatively far from the main star forming centers, shows a clear infall asymmetry, and exhibits only minimal outflow wings that may contaminate any modeling. We find that the $\text{HCO}^+(3-2)$ spectrum at this position does not show any signs of line wings from an outflow. $\text{HCO}^+(1-0)$ does show line wings, which is most likely due to contamination from the IRAS 2A eastern bow shock located $49''$ to the west of $(0''$, $-52''$) (Knee & Sandell 2000). We model the line wings in the $\text{HCO}^+(1-0)$ spectrum with a single gaussian having line center velocity 6.9 km s^{-1} , peak intensity 0.11 K and line width 14.2 km s^{-1} (FWHM). $\text{HCO}^+(1-0)$ and $(3-2)$ spectra at $(0''$, $-52''$) are shown in Figure 5 and the gaussian modeling of the $\text{HCO}^+(1-0)$ outflow is shown as the dotted line.

Because there is outflowing and non-outflowing gas present in the spectrum, it is difficult to separate the two, particularly around 9 km s^{-1} where both are present in significant proportions. We have chosen the gaussian that models the outflow as a best guess based on the following criteria: The $\text{HCO}^+(1-0)$ spectrum closest to the position of the bow shock ($-52''$, $-52''$), which shows the strongest outflow component, is also well modeled by a gaussian with a similar line center velocity and line width, but stronger peak intensity than the outflow gaussian above, plus two peaks corresponding to the red and blue shifted lobes of the self-absorbed profile. The outflow contribution to the $(0''$, $-52''$) spectrum is unlikely to be the dominant source of emission at 9 km s^{-1} because we see emission at this velocity throughout most of Figure 4 excluding the northern part, including positions where there is little or no redshifted outflow emission. For example, spectra at $(26''$, $-52''$) to the east and at $(26''$, $-26''$) to the north-east of $(0''$, $-52''$). Also, Figure 6 shows the HCO^+ emission integrated between 8.5 km s^{-1} and 9.8 km s^{-1} . If we compare this to Figure 4 of Knee & Sandell (2000), which shows a map of the outflow from IRAS 2A, we see that our HCO^+ emission does not show the outflow morphology clearly, therefore we do not consider the outflow is the dominant contributor to the HCO^+ emission over this velocity range.

However, while we consider that the outflow contribution at 9 km s^{-1} is small compared to the non-outflowing gas, it is possible that the outflow contribution is slightly greater than we have modeled. We discuss the implications of this below.

4.2.1. Two-layer model

We fitted each spectrum shown in Figure 5 individually with a simple two-layer model (Myers et al. 1996). The input parameters for the two-layer model are the optical depth (τ), systemic velocity (V_{LSR}), speed at which the two layers are approaching, which is twice the infall speed (V_{IN}), the velocity dispersion (σ), the temperature of the rear layer (T_{R}) and the temperature of the front layer (T_{F}) which we hold constant at 2.73 K. This model matches the “TWOLAYER5” model of De Vries & Myers (2005). The best model and parameters are shown in Figure 5. We find infall speeds and velocity dispersions of 0.06 km s^{-1} and 0.53 km s^{-1} for the (3–2) transition and 0.27 km s^{-1} and 0.70 km s^{-1} for the (1–0) transition of HCO^+ , respectively. We notice that some of the parameters for each fit are different: the infall speed is greater for the (1–0) transition. This is clearly the case as the asymmetry is much greater for the $\text{HCO}^+(1-0)$ spectrum. Also, the velocity dispersion is greater for the (1–0) transition, and the systemic velocity is redder for the (1–0) transition. We note that the systemic velocity obtained by fitting the optically thin $\text{N}_2\text{H}^+(1-0)$ line is 7.03 km s^{-1} . Therefore the systemic velocity determined by the $\text{HCO}^+(3-2)$ two-layer fit (7.412 km s^{-1}) is closer to the optically thin line. A possible explanation for this is that the outflow seen in the $\text{HCO}^+(1-0)$ spectrum has not been accurately removed such that a small part remains within the red shoulder of the $\text{HCO}^+(1-0)$ spectrum, as discussed above. If we have underestimated the contribution of the outflow, then this will have the effect of increasing the modeled infall speed of the (1–0) transition. This is because the weaker red-shifted peak at 9 km s^{-1} will be reduced by a greater proportion than the stronger blue-shifted peak at 6.5 km s^{-1} . Even in the extreme case where all of the emission at 9 km s^{-1} is due to outflow, the blue peak will still be stronger than the (not detected) red peak of the non-outflowing gas. Therefore, we find the result that the (1–0) infall speed is higher than the (3–2) infall speed is robust.

De Vries & Myers (2005) also investigate a “hill” model, which they show results in a better fit of infall speeds than this two-layer model. However, rather than including the hill model here, we use a more detailed radiative transfer model described below.

4.2.2. Radiative transfer model

In order to compare the two-layer model with a more comprehensive model, we use the radiative transfer code RATRAN (Hogerheijde & van der Tak 2000) to simulate emission from the two HCO^+ lines. For our work, we model the emission with 20 concentric shells, each of thickness 10^{14} m . We constrain the density profile of the emitting region to have a flat inner profile and a profile falling off as a power law ($\alpha = -2$) of the radius. We also constrain the central density of the emitting region to be n_c . We hold the radius at which

the turnover occurs (5 shells, or 5×10^{14} m) constant. Such power-law profiles, with a flat inner region, resemble the structure of a self-gravitating isothermal sphere, and have been observed by Tafalla et al. (2004) towards isolated starless cores. Whilst we do not consider inward motions in NGC 1333 to be associated with an isolated starless core, we use this model as a simple approximation.

The simulation allows us to vary infall speed (V_{IN}), the velocity dispersion (σ) and the kinetic temperature (T) for each shell in the emitting region. However, for simplicity, we hold the velocity dispersion and kinetic temperature throughout the emitting region to be constant. Furthermore, we restrict the infall motions to shells 6 to 20 (ie. outside the flat density inner region), which mimicks infall onto a central static core. The radial velocity (V_{LSR}) and the relative abundance of HCO^+ (X) are free parameters. We assume a distance of 300 pc to NGC 1333 (de Zeeuw, Hoogerwerf & de Bruijne 1999; Belikov et al. 2002) and create spectral lines by integrating over the simulated sphere of emission using the same beam size as the FCRAO and CSO observations.

Our best radiative transfer fits are shown in Figure 7. The use of this simple model does not justify a full chi-squared search for the best fitting model. Rather we select the best fits by visual inspection. By varying input parameters around the best fit values, we can estimate uncertainties in each parameter by assessing what appears to be a good fit. We assign an uncertainty of $\pm 0.03 \text{ km s}^{-1}$ to V_{IN} and $\pm 0.05 \text{ km s}^{-1}$ to σ . However, we caution that not all parameters are independent: as discussed below, X and n_c appear to be closely linked. We find that, in the parameter space close to the best fit values, the infall speed and velocity dispersion are independent of other variables.

The values of the parameters shown in Figure 7 are different for the HCO^+ (1–0) and (3–2) lines. This clearly indicates that this model cannot fit the two spectra simultaneously, as was found for the two-layer fits. The reason for this is that the two lines are most likely probing different regions. The most outstanding discrepancy between the fitted parameters is for the value of the infall speed. For the (1–0) line it is 0.77 km s^{-1} and for the (3–2) line it is 0.20 km s^{-1} . This is reflected in the spectra as the asymmetry in the (1–0) line is much more pronounced than the (3–2) line – only the infall speed parameter has a major influence on the asymmetry of the line. As noted in §4.2.1, if we have underestimated the contribution of the outflow in the (1–0) spectrum, then this infall speed may be higher. So again we find that the significant difference between the infall velocities of the (1–0) and (3–2) lines is a robust result. The infall speeds determined using the radiative transfer model are higher than those derived using the two-layer model. We note that De Vries & Myers (2005) have shown that the two-layer model typically underestimates infall speeds by a factor of two, compared to the radiative transfer model. This is in agreement with our findings. A possible reason for

the lower infall speeds with the two-layer model is that it does not take into account the portion of the cloud whose systematic line-of-sight velocity is zero. However, the hill model of De Vries & Myers (2005) suffers from the same limitation, and yet more closely matches the radiative transfer infall speeds. Currently, we are unable to say what is the reason for the discrepancy between these models.

The best fit values of X and n_c each differ by approximately an order of magnitude between the (1–0) and (3–2) lines. However, we note that the simulated spectra obtained by increasing X and decreasing n_c by the same amount have similar shapes, as long as the change is no more than about an order of magnitude. As X is increased and n_c is decreased by the same amount, the overall intensity decreases. The overall intensity is also governed by the kinetic temperature (T), which we have held fixed at 15 K. But if we allow T to vary, it is possible to preserve the line shape by, for example, increasing X , decreasing n_c and increasing T . This implies that, since we do not know the kinetic temperature, the range of best fit values is an order of magnitude for both X and n_c . The values of $10^4 - 10^5 \text{ cm}^{-3}$ for n_c are reasonable considering Tafalla et al. (2004) measured values around 10^5 cm^{-3} in L1498 and L1517B. The relative abundance of HCO^+ of $10^{-9} - 10^{-8}$ agrees with the observationally determined abundance of 2×10^{-9} for IRAS 16293-2422 (Schöier et al. 2002).

Overall, we find that the large number of parameters to fit, as well as the complexity of the best fits suggests that the radiative transfer model is limited in what it can tell us about the gas at the position ($0''$, $-52''$) we have chosen to consider. However, the spectra shown in Figure 7 clearly show a difference in the degree of asymmetry, indicating a difference in the infall speeds measured by the (1–0) and (3–2) lines of HCO^+ . Figure 8 shows the distribution of blue/red peak ratios as a function of infall speed for $\text{HCO}^+(1-0)$ and (3–2), holding all other parameters constant at the best fit values shown in Figure 7. We note that since Figure 7 is produced solely from the radiative transfer model, there is no outflow contamination that might change these results. The infall speed smoothly increases with increasing blue/red HCO^+ ratio up to infall speeds of about 1 km s^{-1} . At higher infall speeds, the blue/red ratio (ie. ratio greater than about 3.5) becomes less sensitive to the infall speed. This is expected because an infall speed of 1 km s^{-1} is about twice the velocity dispersion of the line (0.52 or 0.60 km s^{-1} in our models). Therefore, the front infalling material no longer absorbs the emission from the rear, and the relative intensity of the blue and red components becomes independent of infall speed. So we can only reliably infer infall speeds when the blue/red ratio is below ~ 3.5 .

4.3. Infall speed maps

As can be seen above, the degree of asymmetry of the self absorbed, optically thick line profile is governed by the infall speed, for sufficiently small blue/red ratios. Although we cannot be sure about all the best fit parameters, we can compare relative infall speeds at different positions in the map. From a comparison of the fits to the spectra in Figures 5 and 7, it is difficult to model the emission with simple models. This is mainly because the region is complicated and a simple spherically symmetric model does not adequately represent the region. However, our modeling indicates that the ratio of the blue to red peaks in the spectrum is a good indicator of the infall speed. In both the two-layer and radiative transfer models, only the infall speed appears to significantly affect the ratio of the red and blue peak heights provided the infall speed is less than about twice the velocity dispersion, as discussed in §4.2.2. All other variables may have small effects on the blue/red ratio, but they drastically change the line profile at the same time. Therefore, to preserve a line profile similar to those observed, we assume that only the infall speed is responsible for changes in the ratio. We present maps of blue to red peak ratio for HCO^+ (1–0) and (3–2) in Figures 9 and 10, respectively. The height of each blue and red peak is determined by fitting two gaussians to the line profile and using the height of each gaussian. Where an outflow signature is suspected, a third gaussian was used to remove the outflow contribution, in a similar manner to that discussed on §4.2.

The thick lines shown in Figures 9 and 10 show where infalling motions change to outward motions, particularly around SVS 13 (ie. where the lines are symmetric). The extent of outward motions from both HCO^+ transitions is similar but not identical. This region appears to be larger in the (3–2) transition, compared to the (1–0) transition. This region overlaps with an outflow coming from the SVS 13 region, therefore it is possible that the outward motions we see here are due to swept up material associated with the outflow. Zhou (1995) show that it is possible to have line profiles where the red peak is stronger than the blue peak with a combination of infall and rotation. However, we do not consider this to be the case for SVS 13 because SVS 13 is presumably the central concentration about which any rotation is taking place. At the center of rotation, we would only expect to find an infall profile, where the blue peak is stronger than the red, and yet we find the red peak stronger than the blue at this position.

There is a local maximum of blue/red ratio around IRAS 4. This is clearly seen in both transitions, but is more pronounced in HCO^+ (3–2), which also suggests there may be two centers of high blue/red ratio. We speculate that these two centers may coincide with IRAS 4A and 4B, but the present data is undersampled and we cannot claim this conclusively. This difference in blue/red ratio is more clearly shown in Figure 11, where

the blue/red ratios are shown for a 1-dimensional cut passing through IRAS 4A and 4B. In Figure 11, blue/red peak ratios between 2 and 4, corresponding to infall speeds of 0.4 and 1.0 km s^{-1} , appear to be the norm. However, blue/red peak ratios of up to 7.5 occur at the position of IRAS 4A. As previously mentioned, our model cannot reproduce such high degrees of asymmetry with high infall speeds alone. It is also unlikely that such highly asymmetric line profiles are caused by an increase in optical depth towards IRAS 4 since the self-absorbed profiles are optically thick; our modeling suggests line of sight optical depths of 10 are typical. We believe the outflows in the spectra have been well modeled and are unlikely to be grossly underestimated. In any case, a slight underestimation of the outflow contribution will have the effect of increasing the blue/red ratio. We believe the most likely cause of such highly asymmetric line profiles towards IRAS 4 is an increase in temperature in the inner part of the emitting region. This has the effect of increasing the blue peak of the self-absorbed spectrum, with respect to the red peak. An increase in central temperature is also expected because IRAS 4A and 4B both harbor protostars capable of heating up their immediate surroundings.

Presumably the distinction between 4A and 4B is not seen in the (1–0) map due to lower spatial resolution. If the high blue/red ratios around IRAS 4A/B occur on small spatial scales, then the observed increase in ratios, which is greatest for the (3–2) line around 4A/B, may be partly explained by the lower resolution of the (1–0) map. However, the main reason for the higher blue/red ratios in the (3–2) line is almost certainly because it traces higher density gas than (1–0): we would expect to see the denser gas closer to the protostar(s) and therefore warmer in the center.

The HCO^+ (1–0) map (Figure 9) shows another local maximum of blue/red ratio centered approximately on the position $(-26'', -52'')$, but the (3–2) transition (Figure 10) does not show this. This is also seen in Figure 11, where an increase in blue/red peak ratio up to 5.5 is seen in HCO^+ (1–0), but the blue/red peak ratio of HCO^+ (3–2) remains approximately constant at this position. The nature of this region of increased blue/red ratio is puzzling because it does not occur at any known site of star formation. However, it is $49''$ to the east of the eastern bow shock of the outflow from IRAS 2A (Knee & Sandell 2000). We note that we do not consider the increased blue/red ratio to be an artefact of the outflow because we have removed this component from the spectra. Sandell & Knee (2001) report the detection of a weak continuum source at this position, who suggest it is a result of the bow shock. One possible explanation of this is that the bow shock is a site of triggered star formation and we are seeing the first stages of either increased infall speeds or increased heating as a protostar begins to form. However, one would expect to see an even greater blue/red ratio in the (3–2) transition in this scenario, but this is not the case. In fact, there is no evidence for an increase in blue/red ratio in the (3–2) line at this position. The outflow is red-shifted on this

side of IRAS 2A, so it is possible that the apparent increase in blue/red ratio is an artifact produced by increased red-shifted absorption of the line profile by outflowing material. The lack of evidence for increased (3–2) blue/red ratio is then explained because the density of material in the outflow is not high enough to absorb significant amounts in the $\text{HCO}^+(3-2)$ transition.

It is also intriguing that this region approximately coincides with the position of brightest N_2H^+ emission. Furthermore, whilst Sandell & Knee (2001) note a weak sub-mm continuum source close to this position (SK14), it is much weaker than other sub-mm continuum sources in the field (eg. those associated with IRAS 4A, 4B, 2A and SVS 13). Such a discrepancy between the N_2H^+ brightness and the sub-mm continuum brightness suggests this region may be unusually cold and dense, as N_2H^+ tends to occur in such regions where the main destroyers of N_2H^+ (CO and HCO^+) tend to freeze out onto grains. In order to reduce the speculation, more observations are needed towards this region.

4.4. Extended infall or a cold foreground absorbing layer?

Recently, it has been suggested (Choi et al. 2004; hereafter CKTP04) that the dip in the line profiles seen towards IRAS 4A/B may be due to an unrelated foreground absorber at a systemic velocity of $\sim 8 \text{ km s}^{-1}$. CKTP04 suggest that this foreground layer is extended over a large area, covering at least the regions of IRAS 4A/B and SVS 13. CKTP04 favor the interpretation of a cold foreground layer associated with SVS 13 because the dip seen in their spectra covers a much larger area than just IRAS 4A/B and the emission at the dip velocity appears to peak at the position of SVS 13. We favor the interpretation that the line profiles are indicative of inward motions. If there were a cold foreground layer, then we would expect optically thin N_2H^+ to peak at the same velocity as either the strongest HCO^+ peak or at both HCO^+ peaks. However, N_2H^+ peaks between the HCO^+ peaks, as would be expected for a self-absorbed infall profile. Also, our extended HCO^+ maps indicate that the dip covers an even larger area than previously thought (cf. Figure 3) and is not centered on SVS 13. Furthermore, Figures 9 and 10 show that the infall speed is most likely the highest at IRAS 4A. The absorption dip is not simply deepest at IRAS 4A, which would be consistent with an unrelated foreground screen, but also is reddest at IRAS 4A, which requires a physical association. Also, the extended infall asymmetry that covers most of the field of view in Figures 9 and 10 appears to have a similar velocity as the inverse P-Cygni profiles detected by Di Francesco et al. (2001). We note that Williams & Myers (2000) find a similar extended infall asymmetry towards Serpens. Therefore we consider the dip to be purely the result of self-absorption by a large-scale distribution of physically associated gas

and not due to an unrelated foreground layer.

4.5. Mass infall rates

Previously, Di Francesco et al. (2001) calculated the mass infall rate (\dot{M}_{in}) around IRAS 4A and 4B to be $1.1 \times 10^{-4} M_{\odot} \text{ yr}^{-1}$ and $3.7 \times 10^{-5} M_{\odot} \text{ yr}^{-1}$, respectively. This is based on the measured infall speed (V_{in}), the size of the infalling region (r_{in}), the effective critical density of the transition probing the infall (n):

$$\dot{M}_{\text{in}} = 9.6 \times 10^{-5} \left(\frac{r_{\text{in}}}{0.01 \text{ pc}} \right)^2 \left(\frac{n}{1.3 \times 10^6 \text{ cm}^{-3}} \right) \left(\frac{V_{\text{in}}}{1.0 \text{ km s}^{-1}} \right) M_{\odot} \text{ yr}^{-1}. \quad (1)$$

Using Equation 1 above (Di Francesco et al. 2001), we can measure the mass infall rates for the IRAS 4 system using HCO^+ (3–2), as well as for the major extended infalling region encompassing SVS 13, IRAS 4 and IRAS 2 using HCO^+ (1–0). Effective critical densities are taken from Di Francesco et al. (2001) for H_2CO and from Evans (1999) for the HCO^+ transitions, as shown in Table 1. We calculate infall speeds based on integrated spectra over the regions of interest and use the RATRAN code, described in §§4.2.2. Our mass infall rates are summarised in Table 1.

Perhaps the most striking result shown in Table 1 is that mass infall rates seem to be about the same from the very large scales to the very small (between 3.7 to $11 \times 10^{-5} M_{\odot} \text{ yr}^{-1}$). We caution that this should not be interpreted to mean that all the material infalling on large scales will eventually end up close to IRAS 4A or 4B. This is because we cannot be certain that the infall rate has remained constant throughout time. On the contrary, it is most likely that there have been very different infall rates at other times. Therefore, we note that the similarity of the large scale and small scale infall rates appear to be a coincidence, but this facet of the extended infall in NGC 1333 should be investigated in more detail.

Whilst there appear to be no large differences in the mass infall rates on different scales, we do see a difference between the HCO^+ (1–0) and (3–2) infall speeds on the large scale. Figure 9 shows that the inward motions traced by the (1–0) transition tend to be larger and more widespread than inward motions traced by the (3–2) transition. This suggests that the gas is slowing down at higher densities. Such a decrease in inward motions agrees well with models of collapsing layers (Myers 2005) and collapsing Plummer-like spheres (Whitworth & Ward-Thompson 2001).

The formation rate of stellar mass in NGC 1333 can be crudely estimated by assuming that $\sim 100 M_{\odot}$ have formed in $\sim 1 \text{ Myr}$, giving $\sim 10^{-4} M_{\odot} \text{ yr}^{-1}$, in rough agreement with the estimates in Table 1.

5. Summary and Conclusions

We have observed NGC1333 with the FCRAO in the gas tracers $\text{HCO}^+(1-0)$ and $\text{N}_2\text{H}^+(1-0)$. Our observations cover a large area approximately $15' \times 15'$ ($1.3 \text{ pc} \times 1.3 \text{ pc}$). We have also observed a subset of this region with the CSO in $\text{HCO}^+(3-2)$ in order to trace the higher density gas at a higher spatial resolution. We identify in both $\text{HCO}^+(1-0)$ and $\text{HCO}^+(3-2)$ large areas of red-shifted self-absorption, indicative of infall, covering up to 0.39 pc^2 . These large scale inward motions do not appear to be the result of a superposition of many sites of local infall nor due to absorption of a foreground layer, and suggest this is truly a large scale inward motion of gas. Furthermore, the large scale inward motions appear to be qualitatively different from isolated sites of infall because the global infall speeds are supersonic, whereas local infall speeds are more typically half the sound speed.

We have modeled the HCO^+ red-shifted self-absorption profiles from one position using a simple two-layer model and a more detailed radiative transfer model. This position shows no evidence for outflow in $\text{HCO}^+(3-2)$, and the outflow seen in the $(1-0)$ spectrum is well modeled with a single gaussian. Both models show that the $(1-0)$ and $(3-2)$ emission must come from different regions. This is mainly because the asymmetry in the two spectra are significantly different, implying significantly different infall speeds. The $(1-0)$ line traces a region of higher infall speed (0.77 km s^{-1}) compared to the $(3-2)$ line (0.20 km s^{-1}).

We use the ratio of the blue to red peaks in the HCO^+ spectra as an indication of infall speed over the entire region. The relative infall speed maps show that inward motions dominate the region over approximately the same area in $\text{HCO}^+(1-0)$ and $(3-2)$. The blue/red ratio strikingly increases towards the star forming sites IRAS 4A and IRAS 4B, which is most likely due to an internal heating source at those positions. Outward motions, as evidenced by stronger red peaks than blue peaks, are seen towards SVS 13, which could be the signature of entrained material in the outflows from the SVS 13 region. We find that the mass infall rates appear to be $\sim 10^{-4} \text{ M}_\odot \text{ yr}^{-1}$ on scales from 0.01 pc to 0.32 pc , which is similar to the ratio of the estimated mass of stars in NGC 1333 ($\sim 100 \text{ M}_\odot$) to the cluster age ($\sim 1 \text{ Myr}$).

We would like to thank Susanna Widicus for help with the CSO observing as well as Chris de Vries for generous help with the radiative transfer modeling. We would like to thank an anonymous referee who greatly improved the quality of this paper.

REFERENCES

Bachiller, R., & Cernicharo, J. 1986, *A&A*, 166, 283

- Belikov, A., Kharchenko, N., Piskunov, A., Schilbach, E., & Scholz, R.-D. 2002, *A&A*, 387, 117
- Belloche, A., André, P., Despois, D. & Blinder, S. 2002, *A&A*, 393, 927
- Cernis, K. 1990 *Ap&SS*, 166, 315
- Choi, M., Panis, J. -F., & Evans, N. J. II 1999, *ApJS*, 122, 519
- Choi, M., Kamazaki, T., Tatematsu, K & Panis, J. -F. 2004, *ApJ*, 617, 1157
- Ciolek, G. E. & Basu, S. 2000, *ApJ*, 529, 925
- De Vries, C. H. & Myers, P. C. 2005, *ApJ*, 620, 800
- de Zeeuw, P. T., Hoogerwerf, R., & de Bruijne, J. H. J. 1999, *AJ*, 117, 354
- Di Francesco, J., Myers, P. C., Wilner, D. J., Ohashi, N., & Mardones, D. 2001, *ApJ*, 562, 770
- Evans, N. J., II 1999, *ARA&A*, 37, 311
- Hogerheijde, M. R. & van der Tak, F. F. S. 2000, *A&A*, 362, 697
- Knee, L. B. G. & Sandell, G. 2000, *A&A*, 361, 671
- Lada, C. J., Alves, J. & Lada, E. A. 1996, *AJ*, 111, 1964
- Lee, C. -W., Myers, P. C., & Tafalla, M. 2001, *ApJS*, 136, 703
- Mardones, D., Myers, P. C., Tafalla, M., Wilner, D. J., Bachiller, R. & Garay, G. 1997, *ApJ*, 489, 719
- Mardones, D. 1998, PhD thesis, Harvard Univ.
- Myers, P. C., Bachiller, R., Caselli, P., Fuller, G. A., Mardones, D., Tafalla, M., & Wilner, D. J. 1995, *ApJ*, 449, 65L
- Myers, P. C., Mardones, D., Tafalla, M., Williams, J. P., & Wilner, D. J. 1996, *ApJ*, 465, 133
- Myers, P. C. & Lazarian, A. 1998, *ApJ*, 507, 157
- Myers, P. C., Evans, N., J. II, & Ohashi, N. 2000, in *Protostars & Planets IV*, eds Mannings, V., Boss, A.P., Russell, S. S., (Tucson: University of Arizona Press), 217

- Myers, P. C. 2005, *ApJ*, 623, 280
- Pickett, H. M., Poynter, R. L., Cohen, E. A., Delitsky, M. L., Pearson, J. C. & Muller, H. S. P. 1998, *J. Quant. Spectrosc. & Rad. Transfer* 60, 883
- Nakano, T. 1998, *ApJ*, 494, 587
- Narayanan, G., Moriarty-Schieven, G., Walker, C. K. & Butner, H. M. 2002, *ApJ*, 565, 319
- Ridge, N. A., Wilson, T. L., Megeath, S. T., Allen, L. E., & Myers, P. C. 2003, *AJ*, 126, 286
- Sandell, G. & Knee, L. B. G. 2001, *ApJ*, 546, 49
- Schöier, F. L., Jørgensen, J. K., van Dishoeck, E. F. and Blake, G. A., 2002, *A&A*, 390, 1001
- Shu, F. H. 1977, *ApJ*, 214, 88
- Tafalla, M., Myers, P. C., Caselli, P., & Walmsley, M. 2004, *A&A*, 416, 191
- Walsh, A. J., Myers, P. C. & Burton, M. G. 2004, *ApJ*, 614, 194
- Ward-Thompson, D. & Buckley, H. D. 2001, *MNRAS*, 327, 955
- Williams, J. D. & Myers, P. C. 1999, 511, 208
- Williams, J. D. & Myers, P. C. 2000, *ApJ*, 537, 891
- Wilner, D. J., Mardones, D., & Myers, P. C. 1997, in *AIP Conference Series 393, Star Formation Near and Far : Seventh Astrophysics Conference*, eds Holt, S. S. & Mundy, L. G., (Woodbury N. Y.: AIP Press), 109
- Whitworth, A. P. & Ward-Thompson, D. 2001, *ApJ*, 547, 317
- Zhou, S. 1995, *ApJ*, 442, 685

Table 1. Mass infall rates

Region	infall tracer	effective critical density (cm^{-3})	infall velocity (kms^{-1})	radius (pc)	mass infall rate ($\text{M}_{\odot}\text{yr}^{-1}$)
IRAS 4A	$\text{H}_2\text{CO} (2_{11} - 1_{10})$	1.3×10^6	0.68	0.01	1.1×10^{-4}
IRAS 4B	$\text{H}_2\text{CO} (2_{11} - 1_{10})$	1.3×10^6	0.47	0.01	3.7×10^{-5}
IRAS 4A/B complex	$\text{HCO}^+ (3-2)$	6.3×10^4	0.50	0.06	7.2×10^{-5}
IRAS 4, SVS 13, IRAS 2 region	$\text{HCO}^+ (1-0)$	2.4×10^3	0.60	0.32	1.1×10^{-4}

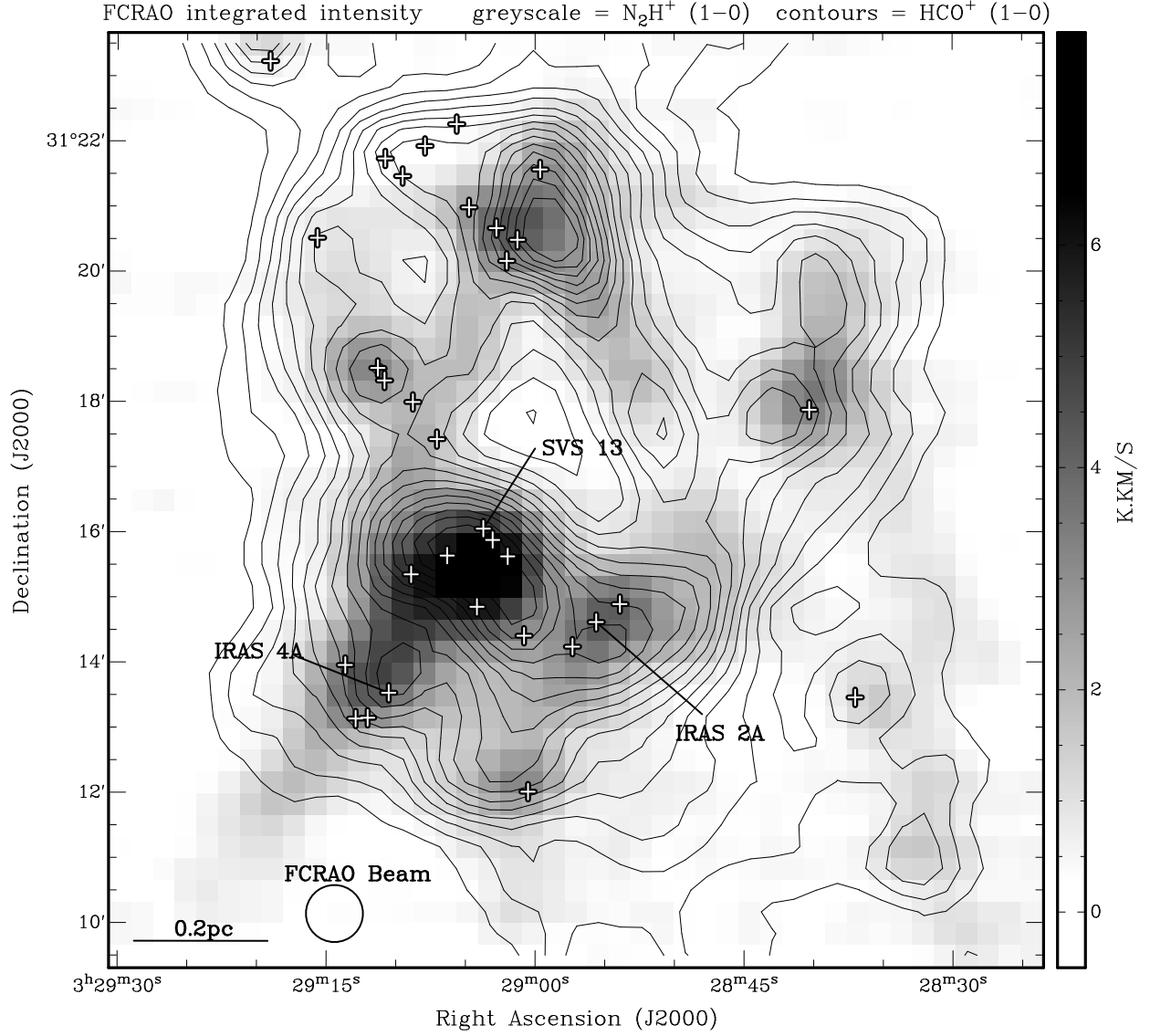


Fig. 1.— Map of NGC 1333. Greyscale is $\text{N}_2\text{H}^+(1-0)$ integrated intensity and contours are $\text{HCO}^+(1-0)$ taken with the FCRAO telescope, on a $20''$ grid. $\text{HCO}^+(1-0)$ contours are 10, 15, 20, 25... 95% of the peak 5.4 K km s^{-1} . The plus symbols represent the positions of dust continuum peaks found by Sandell & Knee (2001).

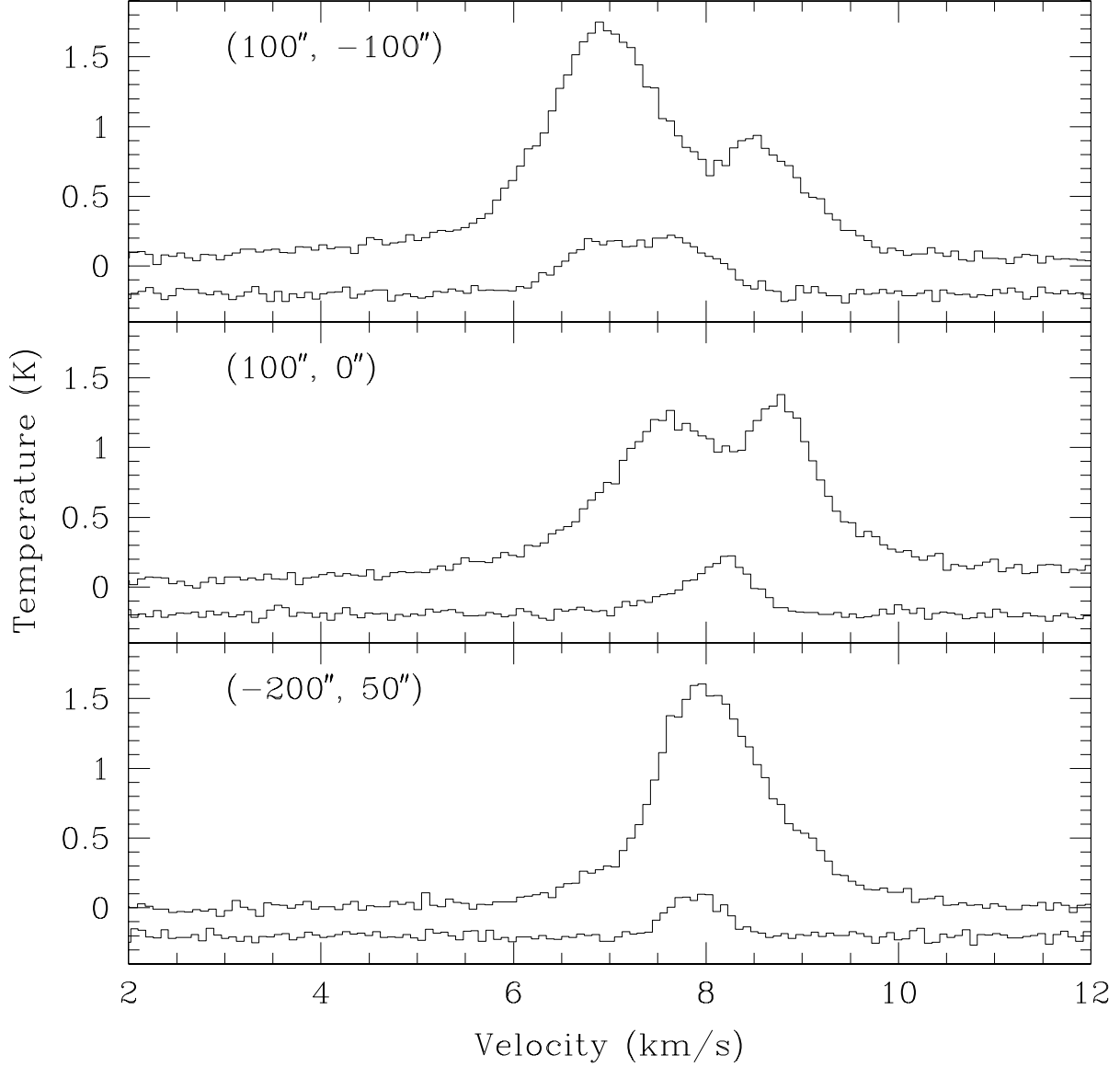


Fig. 2.— Example spectra of HCO^+ (1-0) and N_2H^+ (1-0). For each panel, the top spectrum is HCO^+ (1-0) and the bottom spectrum is the isolated hyperfine line of N_2H^+ (1-0). The top panel shows an example of inward motions, the center panel show an example of outward motions and the bottom panel shows an example where no bulk motions are seen. The (0'', 0'') position corresponds to 03 29 03.9 +31 15 18.9 (J2000).

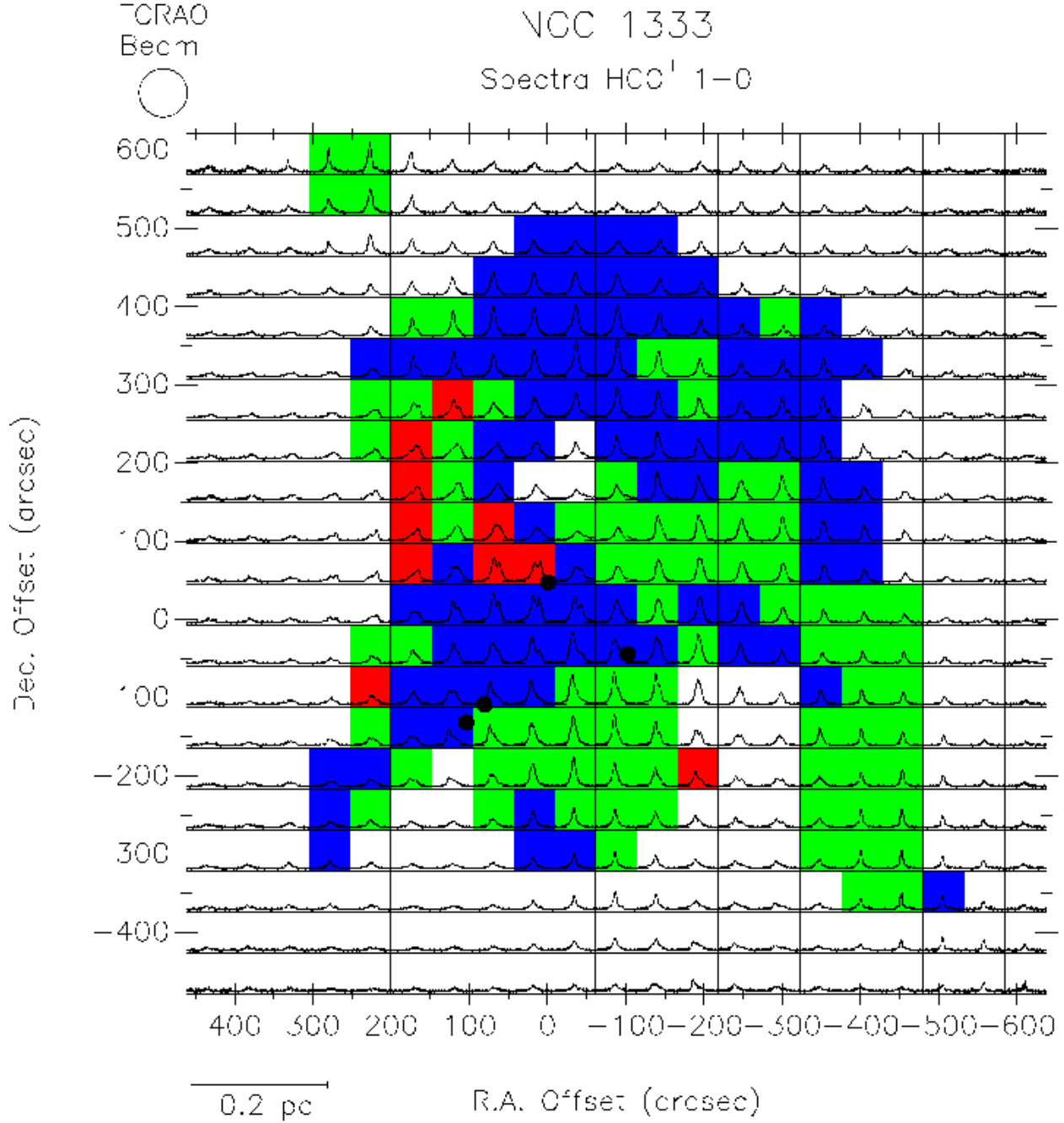


Fig. 3.— Color-coded HCO⁺ (1-0) spectra. Blue spectra indicate regions with $\delta v < -0.25$ (inward motions) and red spectra indicate regions with $\delta v > 0.25$ (outward motions). Green spectra indicate regions where $-0.25 < \delta v < 0.25$ (no clearly defined inward or outward motions). Uncolored spectra indicate regions where the signal-to-noise is too poor to determine δv . The four dots mark the positions of the four main centers of star formation in the southern half of NGC 1333; from north to south: SVS 13, IRAS 2A, IRAS 4A and IRAS 4B. The scales for the HCO⁺ spectra are from 3 to 12 km/s and from -0.2 to 2.5 K (T_{mb}). The (0'', 0'') position corresponds to 03 29 03.9 +31 15 18.9 (J2000).

Fig. 4.— $\text{HCO}^+(3-2)$ (upper) and $(1-0)$ (lower) spectra of the region including IRAS 4, SVS 13 and IRAS 2 in NGC 1333. The $(0'', 0'')$ position is 03 29 3.9 +31 15 18.9 (J2000). The spectra shown in bold are located at $(0'' -52'')$ and are shown in Figure 5

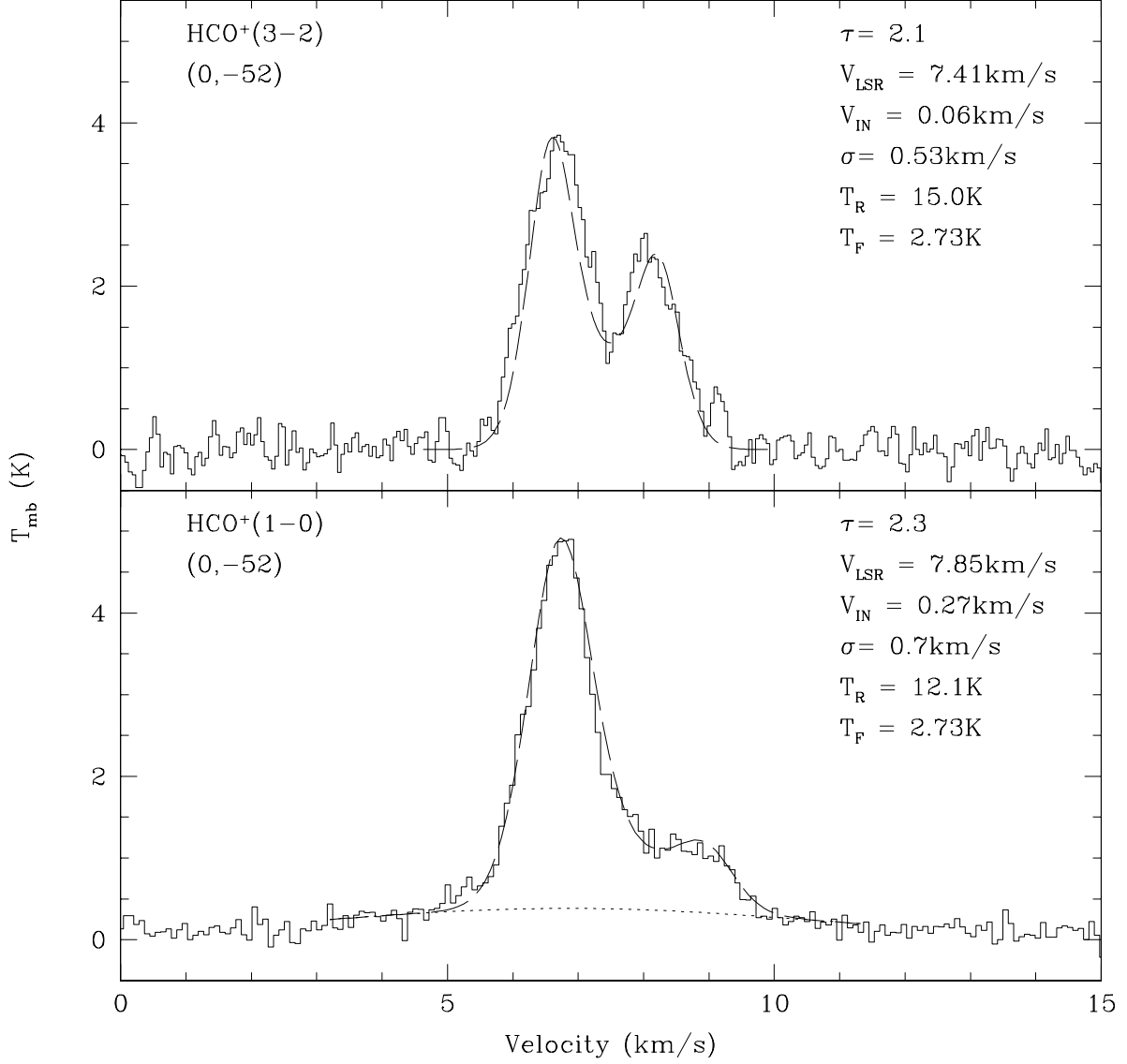


Fig. 5.— $\text{HCO}^+(3-2)$ and $(1-0)$ spectra of the position (0'', -52'') with simple two-layer model fits shown by the dashed line in each. The dotted line in the (1-0) spectrum is a single gaussian fit to the outflow.

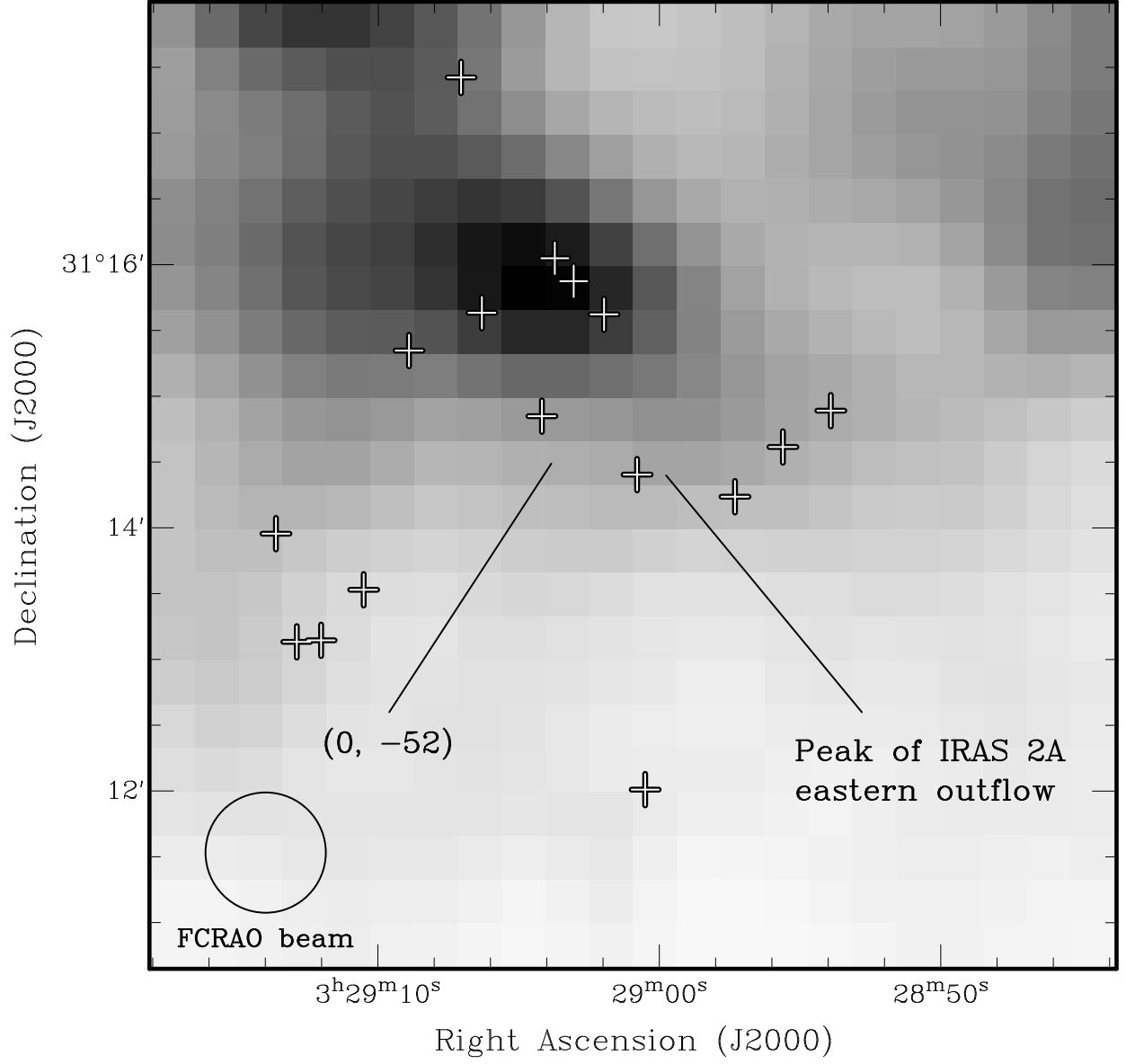


Fig. 6.— $\text{HCO}^+(1-0)$ integrated intensity map between 8.5 km s^{-1} and 9.8 km s^{-1} . The position of the bow shock from the IRAS 2A eastern outflow is shown, but over this velocity range the emission is not dominated by the outflow. The plus symbols represent the positions of dust continuum peaks found by Sandell & Knee (2001).

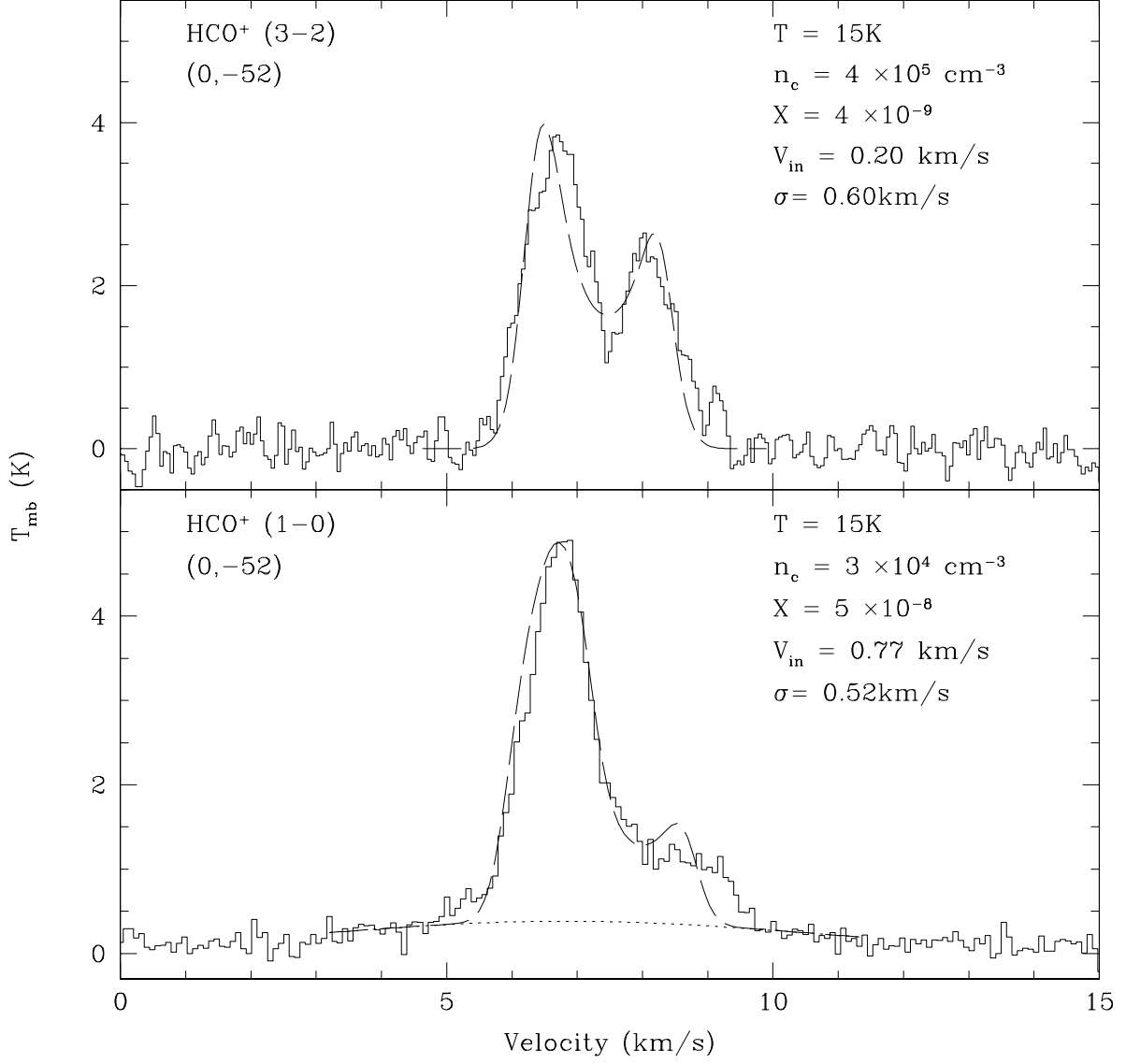


Fig. 7.— HCO⁺(3-2) and (1-0) spectra of the position (0'',-52'') with radiative transfer (RATRAN) fits shown by the dashed line in each. The dotted line in the (1-0) spectrum is a single gaussian fit to the outflow.

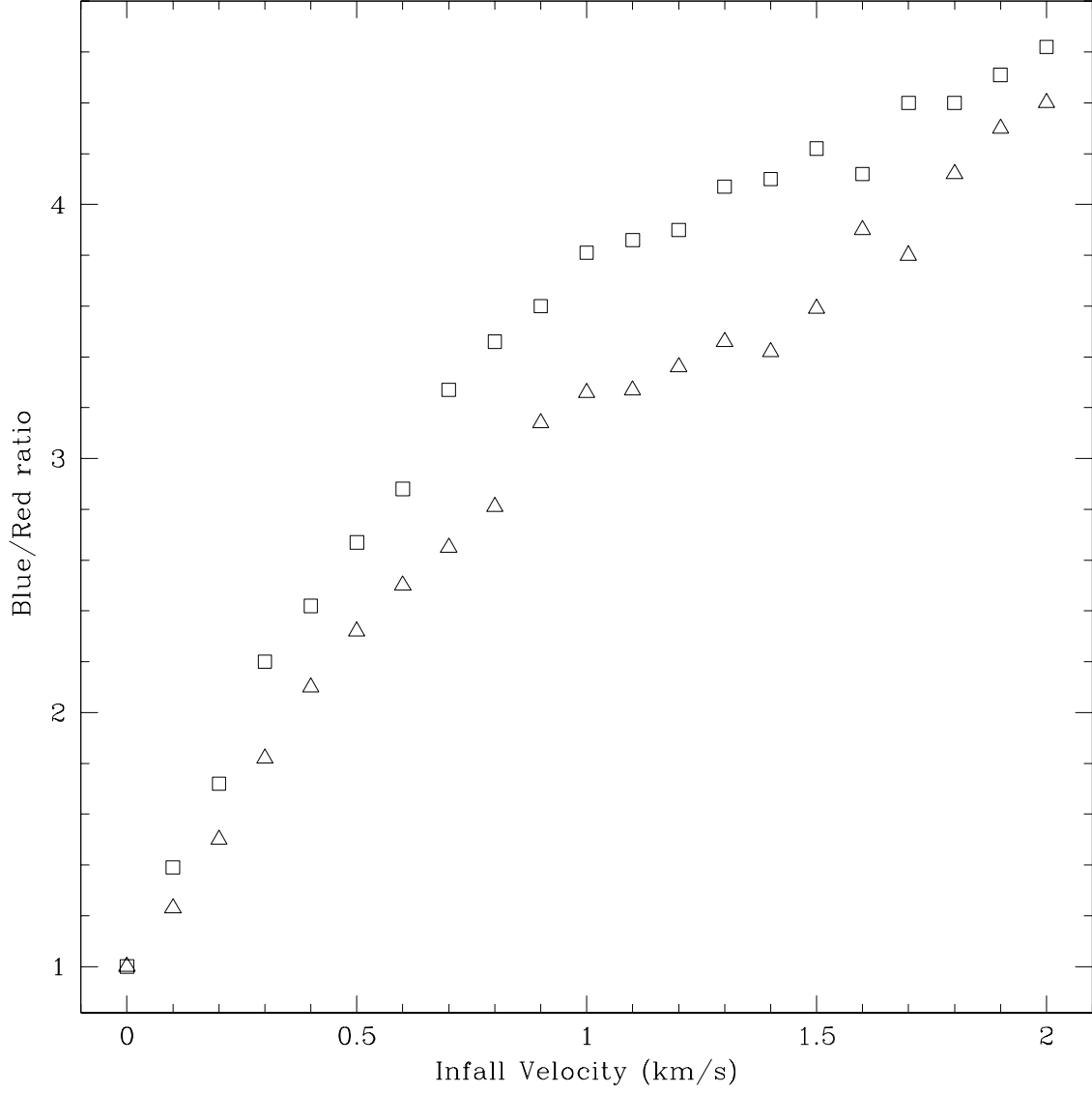


Fig. 8.— Distribution of modeled blue/red peak ratios for various infall velocities. Squares denote models with other parameters that best fit the $\text{HCO}^+(1-0)$ spectrum at $(0'', -52'')$: $n_c = 3 \times 10^4 \text{ cm}^{-3}$, $X = 5 \times 10^{-8}$, $\sigma = 0.52 \text{ km/s}$. Triangles denote models with other parameters that best fit the $\text{HCO}^+(3-2)$ spectrum at $(0'', -52'')$: $n_c = 4 \times 10^5 \text{ cm}^{-3}$, $X = 4 \times 10^{-9}$, $\sigma = 0.60 \text{ km/s}$.

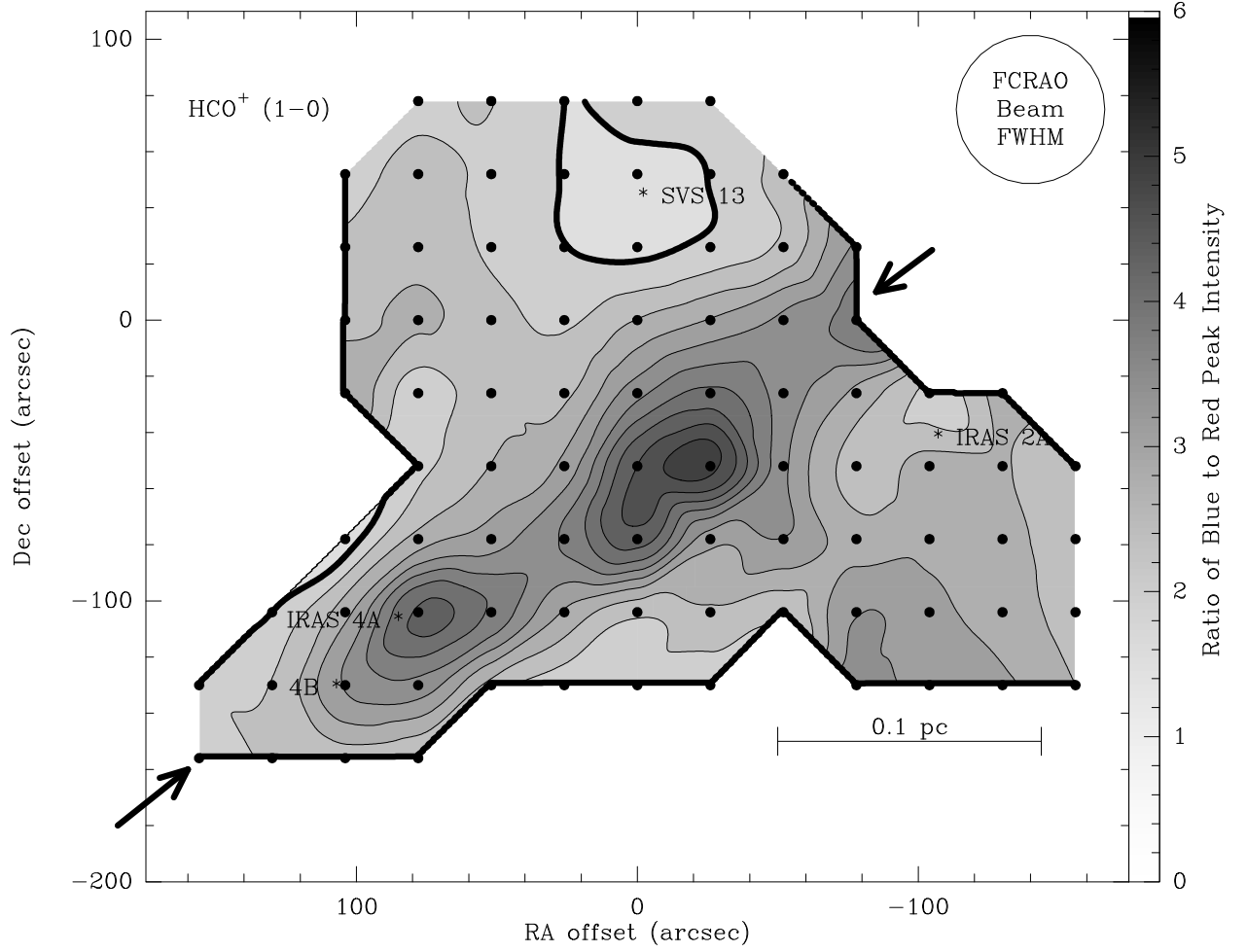


Fig. 9.— HCO^+ (1–0) intensity ratio map. The $(0'', 0'')$ position is 03 29 3.9 +31 15 18.9 (J2000). The thick lines show the contour where the red and blue lines are the same height, ie. no asymmetry. The arrows show the orientation of the cut shown in Figure 11.

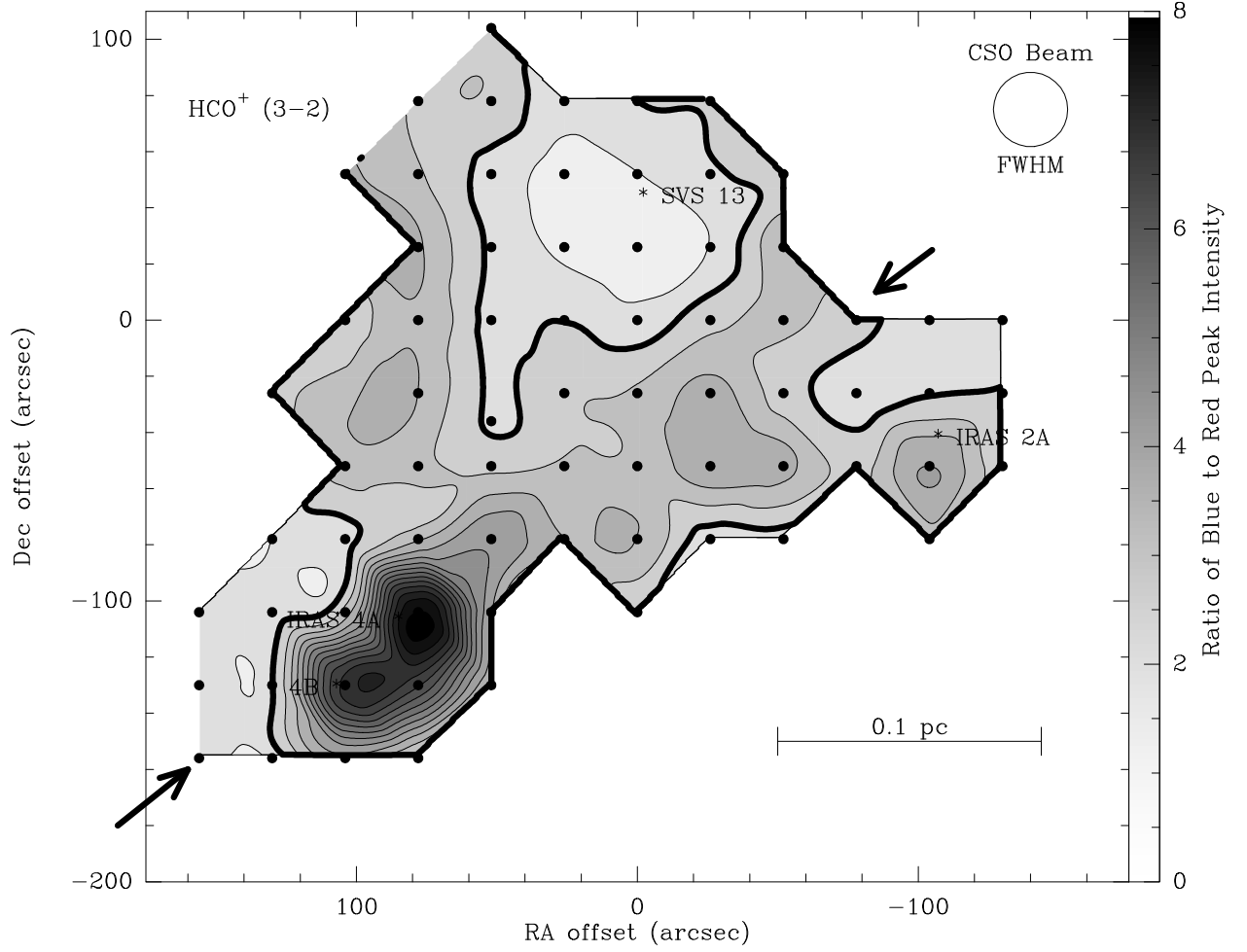


Fig. 10.— $\text{HCO}^+(3-2)$ intensity ratio map. The $(0'', 0'')$ position is 03 29 3.9 +31 15 18.9 (J2000). The thick line shows the contour where the red and blue lines are the same height, ie. no asymmetry. The arrows show the orientation of the cut shown in Figure 11.

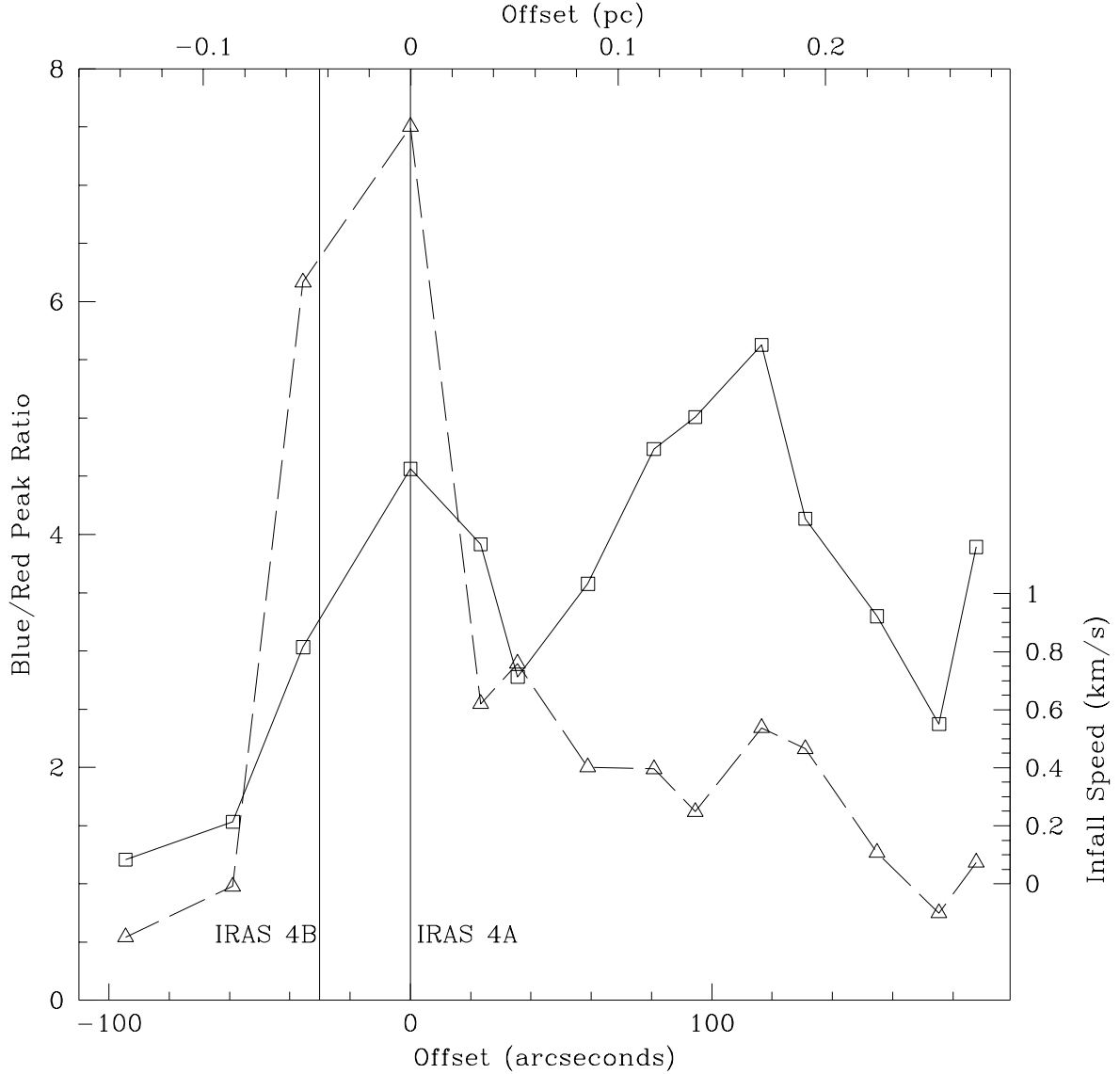


Fig. 11.— Blue/Red HCO^+ ratios. Distribution of blue/red peak intensity ratios for $\text{HCO}^+(1-0)$ is shown as the squares connected by the solid line, and $\text{HCO}^+(3-2)$ is shown as the triangles connected by the dashed line. The positions of IRAS 4A (at the origin) and 4B are marked along the cut. The cut orientation is shown by the arrows in Figures 9 and 10. The right side vertical label shows infall speeds for the range where the blue/red ratio can be reliably used to estimate the infall speed, derived from the HCO^+ (3–2) transition.